

Noname manuscript No.  
(will be inserted by the editor)

---

## Axisymmetric gravity currents in two-layer density-stratified media

R. M. Sahuri · A. K. Kaminski · M. R. Flynn ·

M. Ungarish

Received: date / Accepted: date

**Abstract** Numerous studies have considered the flow of a rectilinear, high Reynolds number, Boussinesq gravity current through a two-layer stratified ambient, however, far less is known concerning the analogue axisymmetric problem. Whereas in both instances there is the possibility of a dynamic coupling between the gravity current front and the waves that are excited by its forward advance, axisymmetric gravity currents entail the added complexity of a radially-diverging flow. Because a steady-state formulation cannot then be developed, we instead present a one-layer shallow water model that describes the flow evolution for various initial conditions and ambient stratifications. We also report upon >30 full- and partial-depth lock release laboratory experiments that span a densitometric range  $0 \leq S < 0.8868$  where  $S = (\rho_1 - \rho_2)/(\rho_c - \rho_2)$  in which  $\rho_c$ ,  $\rho_1$  and  $\rho_2$  denote, respectively, the densities of the gravity current and lower and upper ambient layers.

---

R. M. Sahuri

Dept. of Mechanical Engineering, U. Alberta, Edmonton, AB, T6G 2G8, Canada

(Present address: Spartech Manufacturing, #132 4152 27 St. NE, Calgary, AB, T1Y 7J8, Canada)

A. K. Kaminski

Dept. of Mechanical Engineering, U. Alberta, Edmonton, AB, T6G 2G8, Canada

(Present address: Dept. of Applied Mathematics and Theoretical Physics, Univ. of Cambridge, Cambridge, CB3 0WB, U.K.)

M. R. Flynn

Dept. of Mechanical Engineering and Inst. for Geophysical Research, U. Alberta, Edmonton, AB, T6G 2G8, Canada, E-mail: mrflynn@ualberta.ca

M. Ungarish

Dept. of Computer Science, Technion, Haifa, 32000, Israel

Of principal interest is the initial front speed of the gravity current for which good agreement is observed between laboratory measurement and shallow water numerical simulation, despite the limiting assumptions of the latter. The horizontal distance over which the initial front speed is maintained may span several lock-lengths, however, this depends on whether or not the gravity current is substantially impacted by the interfacial wave(s). For example, when the lower ambient layer is moderate and  $S$  is large, the transfer of momentum from the gravity current front to the wave may lead to a deceleration so severe that gravity current fluid is swept in the  $-r$  direction. The connection between our analysis and problems of pollution dispersion is briefly outlined.

**Key words:** Gravity currents, ambient stratification, interfacial waves, shallow water theory

## 1 Introduction

The flow of a Boussinesq gravity current, a primarily horizontal flow driven by small density differences, through a stratified ambient is a topic that has received notable attention in recent years. Two canonical configurations have attracted the most interest: that of a linearly stratified ambient (Maxworthy et al. 2002, Ungarish & Huppert 2002, Ungarish 2006, White & Helfrich 2008, Goldman et al. 2014) and that of a two-layer ambient (Holyer & Huppert 1980, Rottman & Simpson 1989, Flynn et al. 2012, White & Helfrich 2012). Connecting these two bookend cases are studies such as Tan et al. (2011) that include a thick ambient interface (see also Faust & Plate 1984, Ungarish 2005); a broadening of the interface may reflect, for example, the influence of molecular or turbulent diapycnal mixing.

As with the analogous flow of an intrusive gravity current (Wu 1969, Sutherland et al. 2004, Flynn & Linden 2006, Ungarish 2005), ambient stratification introduces complexity in that internal waves may be excited. Their motion modifies conditions upstream of the gravity current and thereby changes, sometimes quite significantly, the evolution of the flow. Although this effect is well-documented in laboratory experiments (Simpson 1997, section 13.2.1; Tan et al. 2011) and numerical simulations (Maxworthy et al. 2002, White & Helfrich 2008 and 2012) focusing on a rectilinear geometry, comparatively less work has been completed in explaining axisymmetric gravity current motion, some of whose details remain comparatively vague even for the simpler

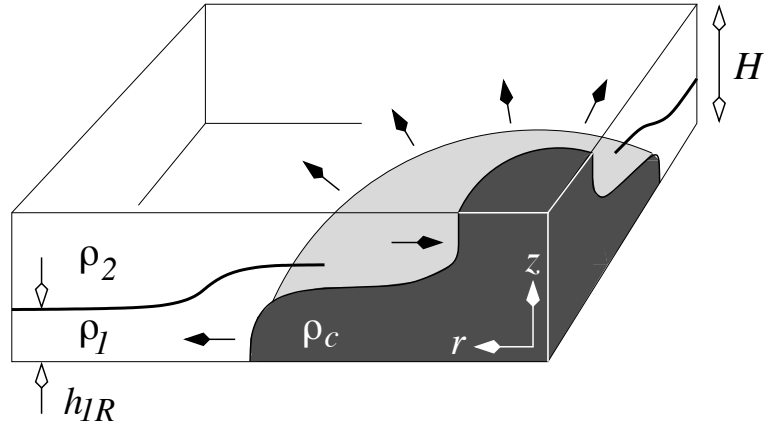


**Fig. 1** Quarter-section view of a radially-expanding axisymmetric gravity current propagating through a two-layer stratified ambient. The schematic shows the experimentally expedient case corresponding to a constant volume release where the initial height of the gravity current fluid,  $h_0$ , matches the channel height,  $H$ , i.e.  $\Xi \equiv H/h_0 = 1$ .

case of a uniform ambient. Notable exceptions include Holdsworth et al. (2012), which describes intrusion flow through a two-layer or continuously-stratified ambient with and without rotation and Chapter 13 of Ungarish (2009), which considers the flow of a rotating axisymmetric gravity current using shallow water and two-dimensional Navier Stokes simulations (the agreement between the two being “consistent... for the initial period of propagation”). Note, however, that Holdsworth et al. (2012) observe nontrivial differences between their measured and predicted front speeds and, in any event, do not examine gravity currents that propagate along a rigid boundary. In addition Ungarish’s exposition is restricted to the case of a linearly stratified ambient and does not include measured data from the laboratory.

So as to fill the gaps identified above, the present study considers the propagation of an axisymmetric gravity current through a two-layer stratified ambient as illustrated schematically in figure 1. The analysis below includes both laboratory experiments and shallow water modeling. (Our models are of shallow water type because they are based on thin-layer, inviscid and hydrostatic approximations.) The analytical treatment separately considers the flow evolution for early- and later-times,  $t$ . When  $t$  is small, it is, as we argue below, acceptable to neglect the geometric curvature terms; an analytical solution that incorporates the details of the ambient stratification may then be derived. Conversely when  $t$  is large e.g. compared to the inertial timescale defined in

§2 below, one must instead solve the shallow water equations numerically using an algorithm specific to hyperbolic partial differential equations e.g. the Lax-Wendroff scheme. Throughout, special attention is devoted to the dynamical influence of the stratification parameter,  $S$ , defined as

$$S = \frac{\rho_1 - \rho_2}{\rho_c - \rho_2}, \quad (1.1)$$

where the fluid densities are defined in figure 1. Also important is the far-field height of the ambient interface, which is given in dimensional and non-dimensional variables as  $h_{1R}$  and  $\varphi = h_{1R}/H$ , respectively, where  $H$  is the total channel height. Finally, because we shall examine finite volume releases, it is of interest to vary the initial height,  $h_0$ , of the gravity current fluid. The associated non-dimensional quantity is  $\Xi = H/h_0$ .

Applications of this work are varied. They include the dispersion of pollution from a concentrated point source in a temperature-stratified lake or the accidental or malicious release of a dense asphyxiating gas in an industrial warehouse or facility where vertical variations of temperature likewise arise.

The remainder of the paper is organized as follows: the experimental equipment and methodology are described in §2. Subsequently, in §3, the shallow water model is presented and (nontrivial) limiting assumptions discussed. A comparison between laboratory measurements and shallow water model predictions is presented in §4. Also included in §4 is a comparison between results germane to axisymmetric and rectilinear geometries, where, in the latter case, data from Tan et al. (2011) are included. Finally, in §5, a series of conclusions as well as ideas for future research directions are outlined.

## 2 Experiments

Laboratory experiments were conducted in a square tank with interior dimensions 120.0 cm long  $\times$  120.0 cm wide  $\times$  29.7 cm tall. A lock gate, cut from a quarter section of a 45.6 cm diameter plastic drum, was located in the front right corner of the tank relative to the camera used for collecting experimental images. Thus the lock radius,  $r_0$ , measured 22.8 cm. A strip of soft neoprene rubber was attached to the sides and base of the gate to minimize, though unfortunately not altogether arrest, leakage. To assist in the even removal of the gate, a pair of wooden guides were affixed

to the tank sidewall. The tank was backlit with either an Electric Vinyl light-sheet or a bank of fluorescent bulbs, the light from which was diffused using plastic sheets.

Experimental runs fell into one of several different categories depending on the values of  $H$ ,  $h_0$  and  $h_{1R}$ . The most straightforward class of two-layer stratified ambient experiments were those of the “full-depth” lock release variety for which  $0 < h_{1R} < h_0 = H$  – see table 1 in Appendix A. Here the tank was first filled to a depth of  $h_{1R}$  with clear fluid of density  $\rho_1$  ranging between about  $1.01 \text{ g/cm}^3$  and  $1.04 \text{ g/cm}^3$ . Dyed fresh water having a density  $\rho_2$  of approximately  $0.999 \text{ g/cm}^3$  was then layered on top using a sponge float to minimize interfacial mixing. The flow of fresh water was terminated once the total fluid depth reached  $H = 20.0 \text{ cm} \pm 0.1 \text{ cm}$ . The lock gate was then lowered into the tank and a preset mass of salt and volume of dye (food coloring) was added to the lock region. Experiments were begun by vertically removing the lock gate, which yielded a gravity current flow of the type illustrated schematically in figure 1. Images were recorded at 4.00 frames-per-second using a LaVision Imager 3 camera ( $1280 \times 1064$ , 12 bit) with a 35 mm Nikon lens. The CCD chip of the camera was located approximately 6.9 m from the front face of the tank. Measurements of the front position were made in a manner similar to previous experimental studies (c.f. Tan 2010 and Tan et al. 2011).

More challenging to conduct were the “partial-depth” lock release experiments for which  $h_0 < H$ . Two scenarios were possible depending upon the magnitude of  $h_{1R}$  relative to  $h_0$ . When  $h_{1R} > h_0$ , we followed a similar procedure to that described above. Here, however, lower layer fluid of density  $\rho_1$  was siphoned from the bottom of the lock after the gate had been lowered. To avoid a difference of free surface elevation between the inside and outside of the lock, upper layer fluid of density  $\rho_2$  concurrently flowed into the lock through a series of four small holes drilled through the gate. The elevation of the holes was approximately 19 cm. Note that the volume of fluid of density  $\rho_1$  removed by siphon was greater than the volume of fluid of density  $\rho_2$  that flowed into the lock, i.e. the free surface elevation, which was equal inside and outside of the lock, decreased during this siphoning step. Once a prescribed volume of fluid had been removed from the tank, the siphon was terminated and an equal volume of dyed fluid of density  $\rho_c$  was added to the bottom of the lock. Fluid addition was done sufficiently slowly (and through a foam-covered nozzle) so that only a small amount of mixing occurred. In the process of adding fluid of density  $\rho_c$ , fluid of density  $\rho_2$

flowed from the lock, through the holes in the lock gate and back into the upper ambient layer, i.e. the free surface elevation, which was again equal inside and outside of the lock, increased during this step and ultimately returned to its original value. Experimental parameters for this category of experiment are summarized in table 2 of Appendix A.

The second category of partial-depth lock release experiment was one wherein  $h_0 > h_{1R}$  – see table 3 of Appendix A. In this case and as described e.g. in Tan (2010), the upper layer of fluid was overfilled by an amount  $\Delta H$ . After plugging the four holes in the gate with plasticine, the gate was lowered into the tank and salt and food coloring were added to the lock region as described above. Before extracting the gate, however, lock fluid of density  $\rho_c$  was first siphoned from the lock bottom. Simultaneously, the plasticine was removed allowing upper layer fluid of density  $\rho_2$  to flow from outside to inside the lock. The siphon was terminated once the free surface elevation was  $H = 20.0 \text{ cm} \pm 0.1 \text{ cm}$  or, equivalently, once  $h_0$  reached its desired value.

For the two types of partial-depth lock release experiments described above, the largest value of  $\Xi$  was 2.51. Running experiments in the limit  $\Xi \gg 1$  was believed to be problematic: large  $\Xi$  requires small  $h_0$ , which in turn suggests a gravity current of small volume and unduly influenced by viscosity – see e.g. (2.1) and (2.2) below.

For reference purposes, and as described in table 4 of Appendix A, we also conducted five control experiments in which the ambient was comprised of a uniform density fluid. These experiments can be thought of as a limiting case, either where  $h_{1R} \rightarrow 0 \text{ cm}$  or  $\rho_2 \rightarrow \rho_1$  and consequently  $S \rightarrow 0$ .

Finally, a limited number of laboratory experiments were conducted in which the backlighting system described above was replaced with a Laser-Induced-Fluorescence (LIF) system. In this way, it was possible to visualize the flow of the gravity current along a thin illuminated slice and to thereby determine more detailed information concerning the structure of the gravity current head. A Litron LPU 350 laser with a beam angle of  $35^\circ$  and producing light at 532 nm was employed. It was placed below the tank and inclined at an angle of  $30^\circ$  relative to the horizontal in order to illuminate the ambient, though not the lock, region. The resulting light sheet ran parallel to the front face of the tank at an offset distance of approximately 1 cm. Accordingly, the lock fluid was dyed not with food coloring but rather with Rhodamine 6G, which had an excitation wavelength of 532 nm corresponding to the incident laser light. The laser and camera were coordinated using

DaVis ver. 8.0. The laser trigger rate was set to 17 Hz and the frame rate was 4.25 frames-per-second.

The inertial timescale associated with the advance of the gravity current front is characterized by  $r_0/\sqrt{g'h_0}$  where  $g' = g(\rho_c - \rho_2)/\rho_2$ . From tables 1 through 4, it is evident that this timescale is typically smaller for full-depth ( $\Xi = 1$ ) than for partial-depth ( $\Xi > 1$ ) lock release experiments. The relative significance of viscosity is assessed by computing a Reynolds number,  $\text{Re}$ , defined by

$$\text{Re} = \frac{h_0}{\nu} \sqrt{g'h_0}, \quad (2.1)$$

and the radius,  $r_v$ , at which viscous effects begin to be important. This latter quantity can be crudely estimated from

$$\frac{r_v}{r_0} = \left( \text{Re} \frac{h_0}{r_0} \right)^{1/6} \quad (2.2)$$

– see (6.58) and §13.3 of Ungarish (2009). The tabulated values for  $\text{Re}$  and  $r_v/r_0$  presented in Appendix A support the hypothesis that the flow is little influenced by viscous dissipation over the range of  $r$  examined here. At least in theory, it is therefore appropriate to compare our measured results against those obtained from a complementary shallow water model where viscosity is likewise ignored. Developing such a model is the topic of the following section.

### 3 Shallow water model

Gravity currents released from a reservoir are inherently time-dependent flows. However, in a rectilinear geometry the front speed and head height during the initial “slumping” stage is time-independent over several lock-lengths, according to the solution of the “dam-break” problem. The flow in the leading bulk can then be modeled by a rectangle of constant height,  $h_N$ , and speed,  $u_N$ , which resembles the steady-state solution derived for rectilinear gravity currents by Benjamin (1968). Axisymmetric gravity currents do not share this feature. The divergence of the streamlines in the axisymmetric outflow from the lock is incompatible with a strict steady-state behavior, i.e. a slumping phase characterized by a leading bulk of constant height and speed. Therefore, even for relatively short propagation distances of  $3r_0 - 4r_0$ , it is appropriate to use a time-dependent model.

Here we apply a one-layer shallow water model. Such an approach has been used before for a variety of related problems; see Ungarish (2007, 2009) and the references therein. To our best

knowledge, however, the present study represents the first application of this model for an axisymmetric gravity current propagating through a two-layer stratified ambient. The advantage of the one-layer shallow water model lies in its mathematical simplicity: a system of partial differential equations of hyperbolic type for the gravity current speed,  $u$ , and height,  $h$ , as functions of  $r$  and  $t$ , which admits realistic initial conditions. The main deficiency is that motions in either ambient layer are ignored. Whereas neglecting this contribution would seem to be imprudent particularly as  $h_0 \rightarrow H$ , (i) we are unaware of a complementary two-layer formulation which can be applied in the present context, and, (ii) one-layer models have proved to be surprisingly resilient in related investigations (e.g. Ungarish 2007, Flynn et al. 2012). More specifically, they have correctly predicted the front speed, at least up until the point where the gravity current motion is strongly influenced by the interfacial wave(s) excited as a result of the collapse and horizontal propagation of the gravity current fluid. Provided that such an interaction is very minor or has not yet occurred and provided also that inertia dominates viscous effects (i.e.  $r_N < r_v$ , where  $r_N$  denotes the radial position of the front and  $r_v$  is given by equation 2.2), there is reason to expect that our model will make credible predictions.

The analysis proceeds along two parallel tracks. Firstly, we present equations suitable for estimating the front speed at early times, i.e.  $t = 0^+$ . Thereafter, we outline a numerical methodology by which the front speed can be estimated for larger  $t$ .

### 3.1 Governing equations and analytical formulation

From this point forward, and unless otherwise noted, it is helpful to non-dimensionalize vertical and horizontal lengths by  $h_0$  and  $r_0$ , respectively, time by  $r_0/\sqrt{g'h_0}$  and speeds by  $\sqrt{g'h_0}$ .

Supposing a “separation of effects,” the front speed,  $u_N$ , depends on the product of two functions, one that incorporates information about the gravity current height and the other which incorporates information about the ambient stratification and gravity current density. In this vein, it is helpful to employ the semi-empirical result of Huppert & Simpson (1980) whereby

$$u_N = \frac{\text{Fr}(a)}{\sqrt{g'h_0}} \times \sqrt{\frac{P_c(z=0) - P_a(z=0)}{\rho_2}}, \quad (3.1)$$

in which  $z = 0$  indicates the bottom of the channel (see figure 1). The Froude number,  $\text{Fr}$ , is given by

$$\text{Fr}(a) = \text{Fr}_{HS}(a) = \begin{cases} 1.19 & 0 \leq a \leq 0.075 \\ 0.5a^{-1/3} & 0.075 < a \leq 1 \end{cases}, \quad (3.2)$$

in which  $a \equiv h_N/H$ . Moreover  $P_c$  and  $P_a$  denote, respectively, the (dimensional) hydrostatic pressure in the current and ambient, which depend on parameters such as the depths and densities of the gravity current and ambient layers – see Flynn et al. (2012) §VI.A. Incorporating these details and simplifying yields the following result:

$$u_N = \begin{cases} \text{Fr}_{HS}(a) \sqrt{1 - S \frac{h_{1R}}{h_N}} \sqrt{h_N} & h_{1R} < h_N \\ \text{Fr}_{HS}(a) \sqrt{1 - S} \sqrt{h_N} & h_N < h_{1R} \end{cases}. \quad (3.3)$$

An alternative expression relating  $u_N$  and  $h_N$  can be derived starting from the mass continuity and radial momentum equations. In matrix form, these read as follows:

$$\begin{bmatrix} h \\ u \end{bmatrix}_t + \begin{bmatrix} u & h \\ 1 - S\hat{H}(h_{1R} - h) & u \end{bmatrix} \begin{bmatrix} h \\ u \end{bmatrix}_r = \begin{bmatrix} -\frac{uh}{r} \\ 0 \end{bmatrix}. \quad (3.4)$$

Here  $h$  and  $u$  denote the depth and speed of the gravity current fluid, respectively,  $r$  is the radial coordinate and  $\hat{H}(h_{1R} - h)$  is a unit step function defined so that

$$\hat{H}(h_{1R} - h) = \begin{cases} 0 & h_{1R} < h \\ 1 & h_{1R} \geq h \end{cases}. \quad (3.5)$$

Employing the method of characteristics for the hyperbolic system described by (3.4), the following characteristic balances can be derived:

$$dh \pm \sqrt{\frac{h}{1 - S\hat{H}(h_{1R} - h)}} du = -\frac{uh}{r} dt, \quad (3.6)$$

on

$$\frac{dr}{dt} = u \pm \sqrt{h[1 - S\hat{H}(h_{1R} - h)]}. \quad (3.7)$$

(Mathematical details are outlined in Appendix A.1 of Ungarish 2009). To close the problem, recall that the gravity current starts from rest. Correspondingly  $u \ll 1$  for  $t = 0^+$  suggesting that the initial dominant balance in (3.6) is between the two terms on the left-hand side of the equation. Integrating (3.6) recognizing that  $u$  must vanish as  $r \rightarrow 0$  then admits the same three possible

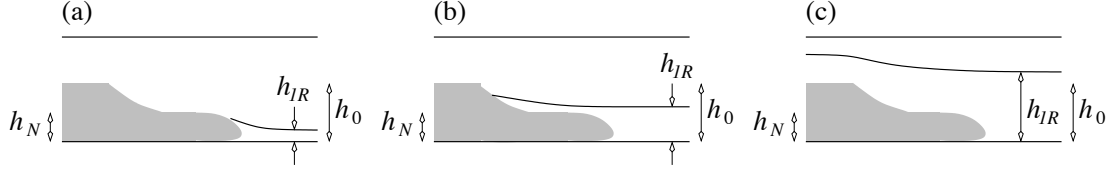


**Fig. 2** The three possibilities admitted by (3.8). In text, vertical length-scales are non-dimensionalized by  $h_0$ . Thus panels (a), (b) and (c), correspond, respectively to  $h_{1R} < h_N < 1$ ,  $h_N < h_{1R} < 1$  and  $h_{1R} > 1$ .

solutions for the front speed,  $u_N$ , as are considered in the rectilinear investigation of Flynn et al. (2012):

$$u_N = \begin{cases} 2(1 - \sqrt{h_N}) & h_{1R} < h_N < 1 \\ 2(1 - \sqrt{h_{1R}}) + 2\sqrt{1-S}(\sqrt{h_{1R}} - \sqrt{h_N}) & h_N < h_{1R} < 1 \\ 2\sqrt{1-S}(1 - \sqrt{h_N}) & h_{1R} > 1 \end{cases} \quad (3.8)$$

(see figure 2). Physically, (3.8) emphasizes that the front speed depends on the initial condition (i.e. the magnitudes of the dimensional variables  $h_{1R}$  and  $h_0$ ). Also important is whether the upper surface of the gravity current is in contact with fluid of density  $\rho_1$ ,  $\rho_2$  or both, the latter alternative being realized when the current depth decreases sharply as a function of  $r$  and the lower ambient layer is not very much deeper than the upper ambient layer (figure 2b).

By combining (3.3) and (3.8), one can determine via iteration the unique solution for a particular ambient stratification/initial condition pair. This solution, consisting of a value for  $h_N$  and a corresponding value for  $u_N$ , is strictly valid only so long as the following conditions are satisfied. Firstly, the right-hand side of (3.6) must be small relative to the two left-hand side terms. (When this condition cannot be assumed to be valid, the more detailed methodology of §3.2 must instead be employed.) Secondly, the ambient interfacial wave that forms at  $t = 0^+$ , propagates into the lock region, is reflected from the origin at  $r = 0$  and then propagates towards the front must not have yet overtaken the gravity current. An estimate for the time,  $t_2$ , associated with this overtaking can be determined as follows. The speed of the interfacial long wave corresponding to the shallow water equations (3.4) is given in non-dimensional variables as

$$u_W = \sqrt{S\varphi(1-\varphi)\Xi}. \quad (3.9)$$

If the front speed,  $u_N$ , is approximately constant up until the point of overtaking, then

$$2 + u_N t_2 \simeq u_W t_2 \quad \Rightarrow \quad t_2 \simeq \frac{2}{u_W - u_N}, \quad (3.10)$$

where the factor of 2 accounts for the fact that the interfacial wave travels from the position of the lock gate to the origin and then back to the lock gate, a dimensional radial distance of  $2r_0$ . The downstream distance associated with overtaking is given by  $u_N t_2$ , where this distance is measured relative to the position of the lock gate. Note also that the estimate for  $t_2$  provided by (3.10) must be regarded as an upper bound: the divergence of the streamlines associated with radial flow implies that  $u_N$  may begin to decrease before the point of overtaking. Finally, note that (3.10) is valid only when  $u_N < u_W$ , i.e. the gravity current is subcritical.

### 3.2 Numerical formulation

To resolve the details of the time-dependent flow, it is necessary to solve (3.4) numerically using a finite-difference Lax-Wendroff method. The boundary conditions are  $u = 0$  at  $r = 0$ , and  $u = u_N$  at  $r = r_N$  where  $u_N$  is given by (3.3). The initial conditions are that the gravity current fluid is stationary within a cylinder of unit radius and height. Note that for  $t = 0^+$ , a steep variation of the gravity current height develops as a result of the forward and backward propagation of the characteristics. The details of this rapid adjustment are modeled using an inclined gravity current interface over two to three grid points about the gate in the first time-step.

For computational convenience, we apply the transformation  $y = r/r_N(t)$ , which maps the  $r \in [0, r_N(t)]$  domain into a constant domain  $y \in [0, 1]$  – see Ungarish 2009 §6.2 and §A.2. A discretization is then applied in  $y$  and  $t$ . The typical grid for the results presented below has a  $1/200$   $y$  interval and a time step of  $2 \times 10^{-3}$ . Tests on finer grids were performed confirming the grid independence of our results. The shallow water code was further verified by evaluating the solution for the short-time initial propagation: in all tested cases, the finite-difference prediction is in good agreement with the analytical result (3.8) at  $t = 0.1$ . For  $\varphi \rightarrow 0$  (vanishing lower ambient layer depth) or  $S \rightarrow 0$  (vanishing density contrast between the two ambient layers) the computed solution reproduces results obtained for the case of a homogeneous ambient. Note also that the finite difference solution for the propagation to  $r_N \approx 5$  requires only modest computer resources.

#### 4 Results and discussion

Figure 3 shows with open symbols laboratory measurements of  $r_N$ , the non-dimensional front position, as a function of non-dimensional time. Panel a considers the special case where  $S = 0$  for  $\rho_c \simeq 1.020 \text{ g/cm}^3$  ( $g' = 20.6 \text{ cm/s}^2$ ) and  $1.057 \text{ g/cm}^3$  ( $g' = 56.9 \text{ cm/s}^2$ ). Also included are numerical results derived from the shallow water model of §3.2 and indicated by the closed diamonds. Over the interval  $1 \leq r_N \lesssim 3$ , variations in the front speed are relatively small, i.e. within the range of experimental error (c.f. McMillan & Sutherland 2010). There is, moreover, a strong overlap between the circles and crosses suggesting that the normalized front speed is approximately independent of  $g'$ . Finally, measured data also display good agreement with the analogue numerical results, as might be expected in the absence of any ambient stratification. For  $r \gtrsim 3.0$ , the front begins to decelerate and there is a mild disparity between the circles and the crosses/diamonds.

In contrast to figure 3 a, which categorizes the impact of  $g'$ , figures 3 b ( $S = 0.30$ ), c ( $S = 0.50$ ) and d ( $S = 0.85$ ) examine the impact of  $S$  and  $\varphi$ . In panel b, the influence of the ambient stratification is comparatively minor: data points corresponding to the different values of  $\varphi$  show a high degree of overlap whether one considers the open or closed symbols. A greater divergence of the data, most notably those from the laboratory, is evident in panels c and d. In the latter case, and when  $\varphi = 0.75$ , the front begins a gradual deceleration after traveling a distance of about one lock radius. Similar comments apply for  $\varphi = 0.50$  although here the deceleration is more pronounced so that the front (i) is fully arrested when  $t \simeq 8.5$ , and, (ii) moves in the  $-r$  direction for  $8.5 \lesssim t \lesssim 11.1$ . For still smaller  $\varphi$ , the dynamic influence of the stratification is qualitatively different. When  $\varphi = 0.25$ , gravity current fluid is co-transported at constant speed by a large-amplitude interfacial wave beyond  $r_N = 3.5$ . (A weaker form of co-transport appears also to be at play for the  $\varphi = 0.25$  data of figure 3 c.)

Real-time experimental videos corresponding to the open symbols of figure 3 d are provided as Electronic Supplementary Material (ESM). For sake of comparison, we also include ESM videos corresponding to the open squares of figures 3 b and c. The videos named `figure3d_opensquare.mpg` and `figure3d_openuptriangle.mpg` affirm that decelerations of the type exhibited in figure 3 d are associated with the overtaking of the front by an interfacial wave and the corresponding trans-

fer of horizontal momentum from the former to the latter. The deceleration is more severe when there is a smaller vertical separation between the ambient interface and the gravity current head. Conversely, the video named `figure3d_opendowntriangle.mpg` corroborates the fact that the gravity current front moves at nearly constant speed when  $\varphi = 0.25$  (and  $S = 0.85$ ). Because of an end-wall reflection of the interfacial wave, it is impossible to predict precisely where or when a sharp deceleration of the gravity current front will occur. It seems likely, however, that this deceleration should be realized for  $r_N \lesssim 4$ . We argue below that video `figure3d_opendowntriangle.mpg` corresponds to a “critical” experiment where the front and interfacial wave speeds are nearly identical. In cases such as these, and consistent with the discussion of Sutherland, Kyba & Flynn (2004), we expect the dynamic coupling between the gravity current and interfacial wave to manifest itself as a comparatively long period of co-transport of gravity current fluid. When, on the other hand, the wave speed appreciably exceeds the front speed, the behavior shown in videos `figure3d_opensquare.mpg` and `figure3d_openuptriangle.mpg` is typical, i.e. the front is relatively quickly overtaken by an interfacial wave or waves leading to deceleration and an irregular pattern of advance.

The general comparison between measured and numerical data in figure 3 is favorable for small  $t$ . As  $t$  increases, however, it is not unusual for the shallow water model to over- or under-predict the measured front position, particularly for large  $S$ . For instance, when  $S = 0.85$  and  $\varphi = 0.25$ , the measured and numerical data begin to diverge for  $t$  as small as 4. We reiterate that the medium and long time evolution of the flow is influenced by factors not accounted for by the shallow water model. These include (i) co-transport or a sharp deceleration of gravity current fluid by interfacial waves, (ii) the presence of a return flow of ambient fluid into the lock region, and, (iii) the possibility of mixing between the gravity current and the ambient layers. Point (i) is reinforced by the fact that  $r_N$  is predicted to increase monotonically in time for  $S = 0.85$  and  $\varphi = 0.50$  whereas the measured results suggest a qualitatively different behavior. Meanwhile the effect of the mixing described in point (iii) is expected to be most pronounced for large  $S$  and small  $\varphi$ : when  $\rho_c \approx \rho_1$  and the lower ambient layer is thin, the propagation is dictated to no small extent by  $\rho_c - \rho_2$  and the head is mostly in contact with the upper layer.

A final comment regarding the ESM videos is that they give the impression of gravity currents whose height is nearly uniform upstream of the front. It is important to recall, however, that

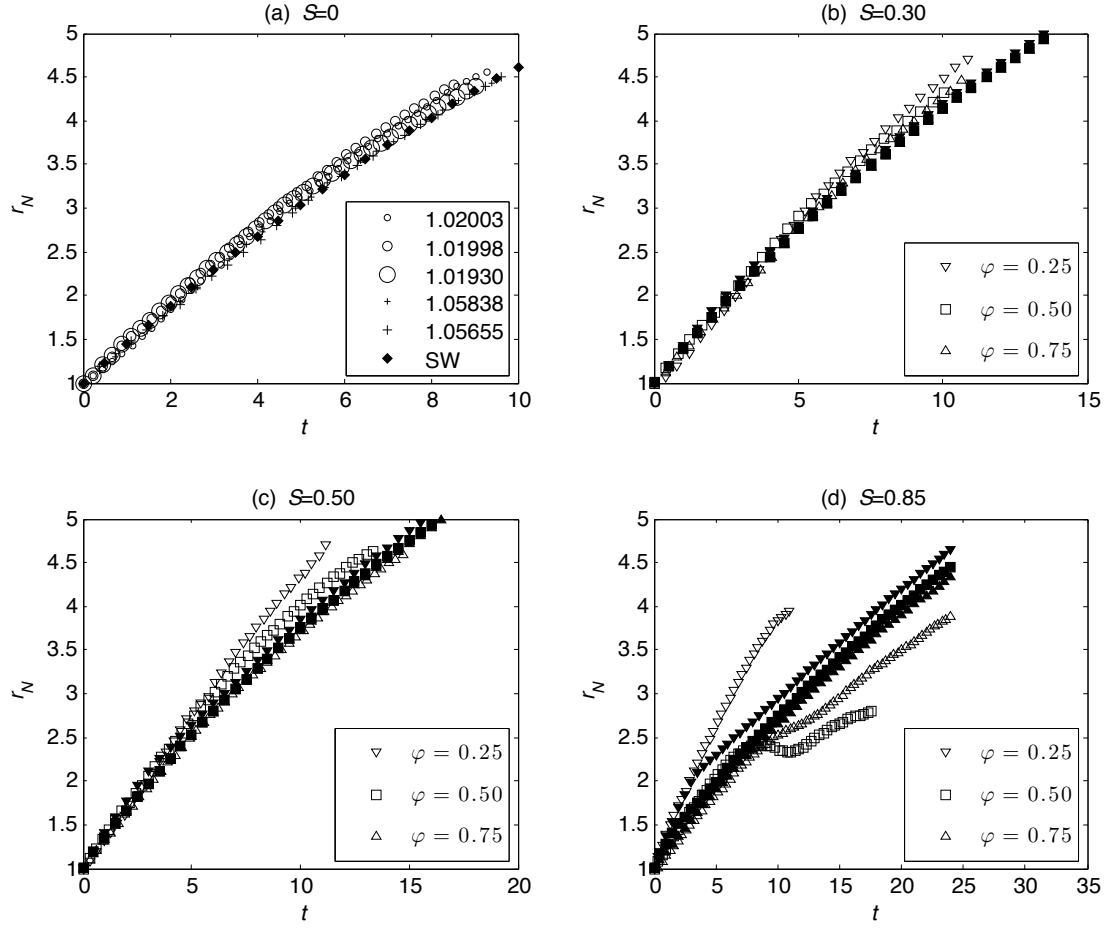


**Fig. 3** Axisymmetric gravity current front position vs. time for  $\Xi = 1$  and various  $S$ . In panel a,  $S = 0$ ; different data points correspond to different values for  $\rho_c$ , whose numerical value (having units  $\text{g}/\text{cm}^3$ ) is specified in the legend. The solid diamonds give the analogue shallow water prediction. In panels b, c and d, the experimental and shallow water results are indicated, respectively, by the open and closed symbols; downward-facing triangles, squares and upward-facing triangles correspond, respectively, to  $\varphi = 0.25$ ,  $0.50$  and  $0.75$ . Panel (b) shows experiments 622, 608 and 618. Panel (c) shows experiments 621, 629 and 615. Panel (d) shows experiments 627, 613 and 628; experimental data sets are truncated at the point where end-wall reflections of the interfacial wave nontrivially impact the advance of the gravity current front. Vertical error bars have a length less than or equal to the height of the data point symbols.

the ESM videos project a radial flow occurring in the quarter-plane into a single plane, namely that which is aligned with the front face of the tank (see figure 1). A more precise picture of the structure of the gravity current head is offered by the LIF experimental images. Consistent with the discussion of §2, these show the flow along a single illuminated radial slice. Figure 4 presents a sequence of LIF images where the experimental parameters coincide with those of the open squares

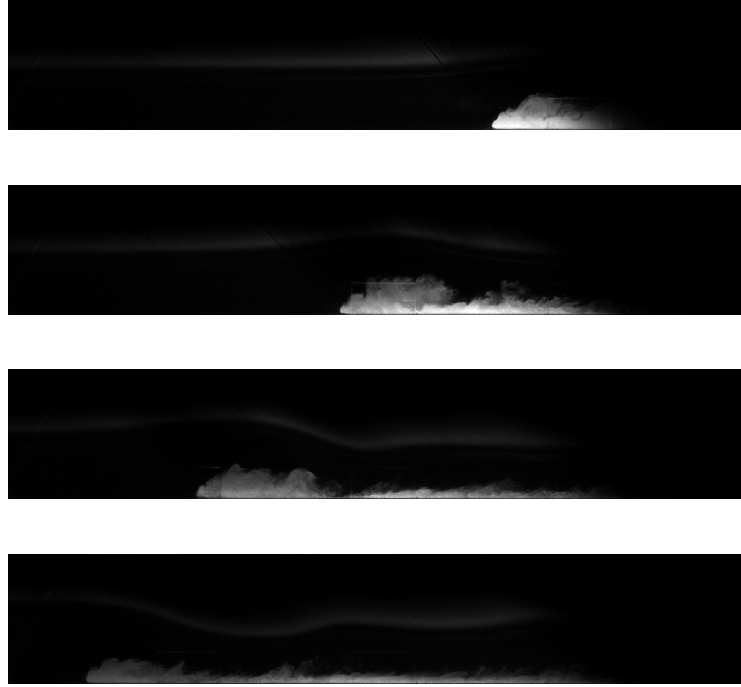


**Fig. 4** LIF experimental image showing the evolution of an axisymmetric gravity current (full depth-lock release). Here  $\varphi = 0.50$ ,  $\Xi = 1.0$  and  $S = 0.5235$  ( $\rho_c = 1.03816 \text{ g/cm}^3$ ,  $\rho_1 = 1.01930 \text{ g/cm}^3$ ,  $\rho_2 = 0.99858 \text{ g/cm}^3$ ). The dimensional time interval,  $\Delta t$ , between successive panels, which measure 110.6 cm long by 20.0 cm tall, is 2.88 s ( $\Delta t \sqrt{g' h_0} / r_0 = 3.52$ ). Although we did not specifically add fluorescent particles to the ambient interface, its outline is visible, albeit only faintly.

from figure 3 c – see also the ESM video named `figure3c_opensquare.mpg`. The LIF images confirm that the axisymmetric gravity currents realized in our laboratory experiments exhibit a familiar raised head whose height generally decreases with time. Figure 4 further suggests that the interface between the head and the lower ambient layer is characterized by considerable shear.

Whatever the differences between the data sets exhibited in figure 3 and whether or not the shallow water numerical solutions provide meaningful predictions for large  $t$ , one can in each case estimate an initial front speed associated with the advance of the gravity current. Corresponding data are shown in figure 5 which presents  $u_N$  as function of  $S$  for  $\Xi = 1$  and  $\varphi = 0.25, 0.5$  and  $0.75$ . For the case of the laboratory experimental data (open circles),  $u_N$  is computed by determining the slope of the associated least-squares line of best fit. Such curve fitting is, of course, limited to the range where the front speed is approximately constant and therefore excludes data points corresponding to the deceleration of the flow. A similar methodology for computing the front speed

was applied in the rectilinear experiments conducted by Tan et al. (2011); select data from Tan et al.'s investigation are indicated by the crosses. Conversely the closed circles show the predictions of the axisymmetric shallow water model described in §3.2 and correspond to the average front speed measured over  $1 \leq r_N < 2$ . These data are therefore different, in general, from the predictions obtained by the simultaneous solution of (3.3) and (3.8). The latter results are indicated by the solid curves and correspond to the front speed at  $t = 0^+$  i.e.  $r_N = 1^+$ .

The overall degree of overlap between the different data sets exhibited in figure 5 is favorable. Because (3.3) and (3.8) deliberately omit adjustment effects associated with the removal of the lock gate (and the rapid, though not instantaneous, acceleration of the fluid of density  $\rho_c$ ) or the subsequent deceleration of the gravity current front, the solid curves lie above the closed circles, where such effects are included. The offset is small, however, particularly for modest  $S$ . Also, there is a high degree of overlap between the open and closed circles suggesting that effects ignored in §3 such as entrainment/detrainment, viscosity and the return flow into the lock region do not exert a leading-order influence on the initial front speed.

In each of the panels of figure 5,  $u_N$  decreases with  $S$ . This observation is consistent both with the corresponding rectilinear flow (see e.g. figure 9 of Tan et al. 2010) and also with physical intuition: for fixed  $\rho_c$  and  $\rho_2$ , larger  $S$  is associated with a larger average ambient density and therefore a decreased driving force for flow of the type illustrated schematically in figure 1. Note, moreover, that the solid curves drawn for different  $\varphi$  converge as  $S \rightarrow 0$ . (Similar remarks apply also to the data points.) In the limit as  $S \rightarrow 0$ , the ambient consists of fluid of a single density rather than an upper and lower layer with  $\rho_1 > \rho_2$ . For finite  $S$ ,  $u_N$  decreases as  $\varphi$  (and hence the depth-average ambient density) increases. This result is again consistent with the behavior noted in rectilinear channels.

Finally, the dashed curves of figure 5 show the interfacial long wave speed as specified by (3.9). To the left (right) of the intersection point of the dashed and solid curves, the gravity current is classified as supercritical (subcritical). The shaded areas are based on (3.3), (3.8), (3.9) and (3.10); they indicate the parametric region where the interfacial wave is predicted to overtake the gravity current front before the latter reaches the far end wall of the tank. (Obviously, the left boundary of this shaded area must lie to the right of the intersection point between the dashed

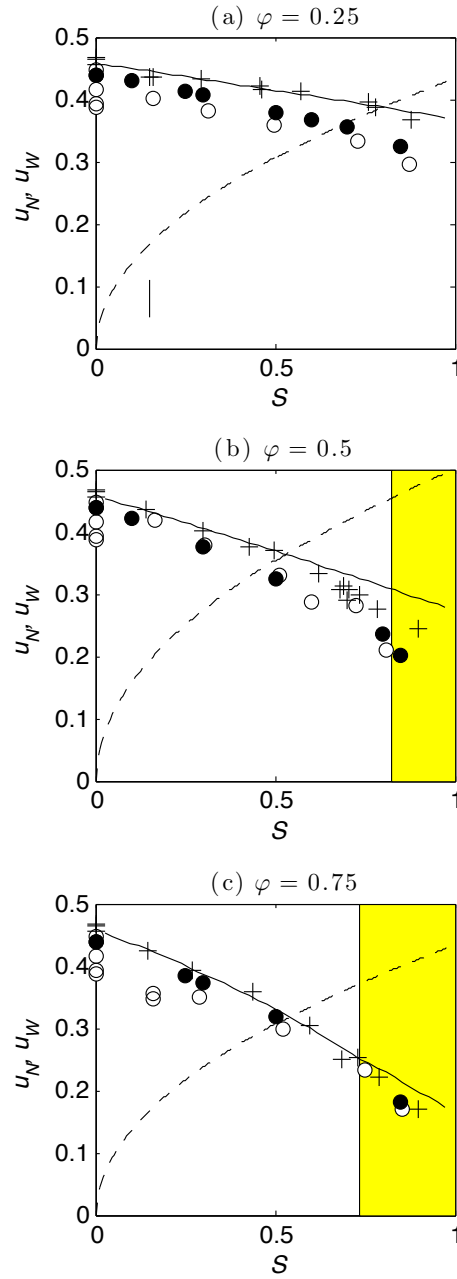


**Fig. 5** [Color] Axisymmetric gravity current front speed vs.  $S$  for  $\Xi = 1$  and various  $\varphi$ . Open and closed symbols correspond, respectively, to laboratory measurements and shallow water numerical simulations. Crosses show analogue rectilinear data and are drawn from Tan et al. (2011). The solid curves indicate the solution of (3.3) and (3.8) whereas the dashed curves show  $u_w$  predicted by (3.9). Moreover, the shaded areas in panels b and c indicate the regions where, based on the analytical solutions and (3.10), overtaking of the gravity current front by the ambient interfacial wave will occur before the front reaches the tank end wall. Finally, a maximal error bar corresponding to the open circles is shown in the lower left hand corner of panel a.

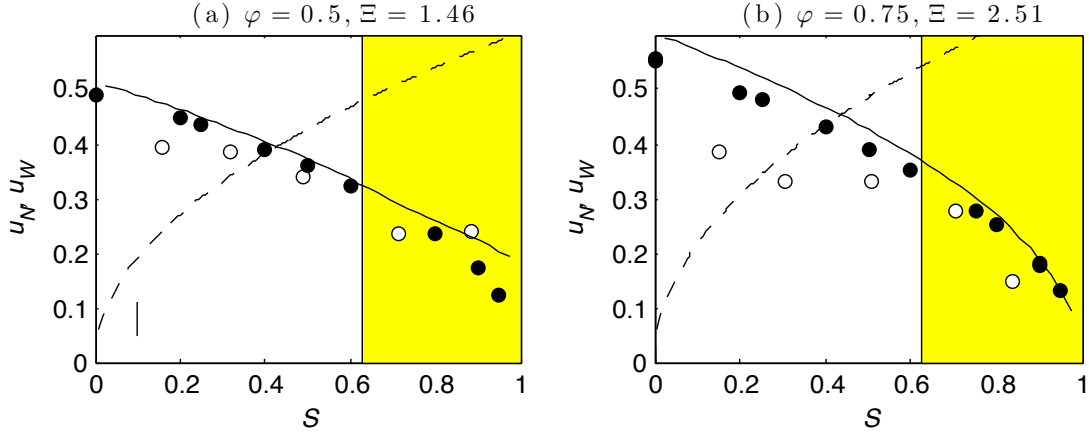


**Fig. 6** [Color] Axisymmetric gravity current front speed vs.  $S$  for  $\Xi > 1$ . (a)  $\varphi = 0.5$ ,  $h_0 > h_{1R}$ ,  $\Xi = 1.46$  and (b)  $\varphi = 0.75$ ,  $h_0 < h_{1R}$ ,  $\Xi = 2.51$ . Symbols, lines and shaded areas are the same as in figure 5. A maximal error bar corresponding to the open circles is shown in the lower left hand corner of panel a.

and solid curves.) Importantly, the shaded regions are broadly consistent with the data provided in figure 3. When  $S = 0.3$ , for example, overtaking is predicted not to occur because the gravity currents are supercritical for  $\varphi = 0.25$ ,  $0.5$  and  $0.75$ . Correspondingly in figure 3 b, the front speed is approximately constant. A different prognosis arises when  $S = 0.85$  (corresponding to figure 3 d) for which overtaking is anticipated when either  $\varphi = 0.50$  or  $0.75$ , but not  $0.25$ . In fact, and as noted above,  $S = 0.85$ ,  $\varphi = 0.25$  corresponds to a nearly critical case in which the wave and front speeds are predicted to be almost identical ( $u_W = 0.399$ ,  $u_N = 0.383$ ). In such a scenario, we expect the co-transport of gravity current fluid by the interfacial wave to be especially effective. This conjecture is consistent with the downward facing triangles of figure 3 d, which show a constant front speed till  $r_N \gtrsim 3.5$ . The  $S = 0.5$  case is more nuanced. Here again, no overtaking is predicted (or observed) for any of  $\varphi = 0.25$ ,  $0.5$  and  $0.75$ . When  $\varphi = 0.25$ , figure 3 c suggests co-transport, albeit of a much more limited variety than occurs when  $S = 0.85$ . On the other hand, the interfacial wave speed of  $u_W = 0.306$  anticipated from (3.10) falls below both the predicted ( $u_N = 0.414$ ) and experimentally measured ( $u_N = 0.357$ ) values for the front speed. This comparison serves as an important reminder of one of the key assumptions associated with (3.10), namely that the interfacial wave is a linear long wave having negligible amplitude. Although related rectilinear studies such as Tan et al. (2011) and White & Helfrich (2012) have considered nonlinear interfacial waves/disturbances, we do not pursue this line of inquiry here.

Data corresponding to figure 5 but with  $\Xi > 1$  are presented in figure 6. Although the level of agreement between the experimental and the shallow water results remains generally favorable, some nontrivial deviations are noted, particularly for small  $S$ . The most likely explanation for this discrepancy is that, as we describe in §2, the experimental setup is more involved when  $\Xi > 1$  and this affords more opportunity for fluid leakage across the gate, particularly when  $S$  is small and the difference between  $\rho_c$  and  $\rho_1$  large. When such leakage occurs, the assumed initial and upstream conditions no longer apply; rather the ambient is characterized by a thin lowermost layer of approximate density  $\rho_c$  whose impact is to increase the average ambient density and consequently depress  $u_N$ . Note moreover that the data of figure 6 a,b do not coincide as  $S \rightarrow 0$  because the corresponding  $\Xi$  values differ by a nontrivial amount.

Similar to figure 5, the shaded areas of figure 6 indicate the parametric range where overtaking of the gravity current front is predicted via (3.10). As anticipated, the shaded region of figure 6 a is wider than that of figure 5 b and likewise when comparing figures 6 b and 5 c. For fixed  $\varphi$ , overtaking is therefore expected for a broader interval of  $S$  values as  $\Xi$  increases.

## 5 Conclusions

The present analysis considers axisymmetric gravity current flow through a two-layer stratified ambient corresponding to a finite volume release. To our best knowledge, the laboratory experiments described in §2 represent the first physical experiments modeling this type of flow. Both they and the analogue shallow water numerical simulations of §3 assume the gravity current fluid to be more dense than either of the ambient layers. Provided the system is Boussinesq, however, entirely equivalent results are expected for the case where  $\rho_c < \rho_2 \leq \rho_1$  (fluid densities are defined in figure 1). Moreover and as suggested by the data of tables 1 through 4 (Appendix A), we focus on high-Reynolds number gravity currents that are, to leading order, unaffected by viscosity. The inviscid nature of the flow is consistent with (2.2) and our calculation of the radial distance,  $r_v$ , at which viscous effects should begin to exert a notable impact. For the present experiments,  $r_v$  typically exceeds the tank length.

The flow evolution is principally governed by the following three non-dimensional parameters:  $S$ , defined by (1.1),  $\varphi = h_{1R}/H$  and  $\Xi = H/h_0$  (length-scales are defined in figure 1). Small  $S$

yields large front speeds so that the gravity current is not quickly overtaken by an interfacial wave. Conversely, when  $S$  is large, there may be a substantial transfer of horizontal momentum between the front and the interfacial wave leading to pronounced deceleration of the gravity current. In extreme cases e.g. when  $\varphi$  is moderate, the deceleration may be so severe that the front is pushed in the  $-r$  direction over a significant distance (see e.g. the open squares of figure 3 d and the ESM video `figure3d_opensquare.mpg`).

A major focus of our investigation is to present a novel comparison of the initial front speed measured in the laboratory with that predicted from shallow water theory. In the latter case, it is possible to derive an analytical solution for the front speed at the initial instant,  $t = 0^+$ , as we do in §3.1. Alternatively, and as suggested by the discussion of §3.2, one may numerically solve the shallow water equations and thereby compute the average front speed over some interval e.g.  $1 \leq r_N < 2$  where  $r_N$  denotes the front position. In either case, a one-layer shallow water model is employed because, to our best knowledge, there is no corresponding two-layer model that can be applied in the present circumstance. Figures 5 and 6 indicate that such a one-layer model yields generally accurate predictions for the initial front speed. This encouraging observation is in line with related investigations such as Ungarish (2007), which likewise attest to the surprisingly robust nature of the one-layer shallow water model despite its omission of ambient return flows, mixing and viscous dissipation. Of course, one-layer shallow water models also ignore ambient interfacial waves. As suggested above, these waves may exert a dynamically-significant effect leading either to the sudden deceleration of the front for relatively modest  $r_N$  or, alternatively and for smaller  $\varphi$ , to co-transport of gravity current fluid over comparatively longer distances. So although the present one-layer shallow water model has been shown to be effective in computing the initial front speed, other more detailed tools such as Direct Numerical Simulation are required to reliably resolve the later time flow dynamics. This is particularly true when  $S$  is large and the interfacial wave may be especially effective at extracting horizontal momentum from the gravity current front. The above conclusion complements observations from studies of rectilinear gravity current flow through either two-layer or linearly-stratified ambients – in particular, see figures 12.3 and 12.6 of Ungarish (2009) and the discussion thereof.

Applications of our work are several-fold, but pertain most directly to problems of pollution dispersion e.g. in stratified water bodies characterized by a two-layer stratification where  $\varphi$  is neither very nearly zero or unity. In this case, it is necessary from the point of view of environmental planning to predict the extent to, and timescale over, which pollution appears at various locations downstream of the source. Future topics to be addressed include assessing the influence of a symmetry-breaking mean flow, modifying the source details so that there is a constant flux of gravity current fluid and adding topographic features along the bottom boundary. The latter topic in particular has received comparatively little attention and is one that is presently being investigated in our laboratory.

#### *Acknowledgments*

Financial support was generously provided by NSERC through the Discovery, USRA and RTI Grant programs. The tank used in the experimental portion of this study was fabricated in the Dept. of Mech. Eng. Machine Shop at the Univ. of Alberta. The ESM videos were produced with the kind assistance of Mr. Esmatullah Naikyar.

#### **A Experimental data**

Tables 1 through 4 present the experimental parameters pertinent to the measured data discussed in §4. Consistent with the discussion of §2,  $h_0$ ,  $r_0$  and  $r_v$  are dimensional quantities, the latter of which is determined from (2.2). The associated Reynolds number is defined by (2.1). In all cases, fluid densities were measured using an Anton Paar 4500 densitometer having an accuracy of  $\pm 0.000005 \text{ g/cm}^3$ .

#### **References**

1. T. Maxworthy, J. Leilich, J. Simpson, and E. H. Meiburg. The propagation of a gravity current in a linearly stratified fluid. *J. Fluid Mech.*, 453:371–394, 2002.
2. M. Ungarish and H. E. Huppert. On gravity currents propagating at the base of a stratified fluid. *J. Fluid Mech.*, 458:283–301, 2002.
3. M. Ungarish. On gravity currents in a linearly stratified ambient: A generalization of Benjamin’s steady-state propagation results. *J. Fluid Mech.*, 548:49–68, 2006.
4. B. L. White and K. R. Helfrich. Gravity currents and internal waves in a stratified fluid. *J. Fluid Mech.*, 616:327–356, 2008.

**Table 1** Laboratory experimental data for  $\Xi = 1$ .

Expt.	$\varphi$	$\rho_c$ (g/cm <sup>3</sup> )	$\rho_1$ (g/cm <sup>3</sup> )	$\rho_2$ (g/cm <sup>3</sup> )	$S$	$\sqrt{g/h_0}$ (cm/s)	$\frac{\tau_0}{\sqrt{g'h_0}}$ (s)	Re ( $\times 10^4$ )	$\frac{\tau_c}{\tau_0}$
626	0.25	1.06191	1.00901	0.99891	0.1603	35.2	0.649	7.03	6.29
622	0.25	1.06754	1.02069	0.99909	0.3156	36.6	0.622	7.33	6.33
621	0.25	1.04209	1.02069	0.99899	0.5035	29.1	0.784	5.82	6.09
625	0.25	1.02861	1.02055	0.99884	0.7293	24.2	0.943	4.83	5.91
627	0.25	1.04313	1.03748	0.99896	0.8721	29.4	0.775	5.89	6.10
612	0.50	1.06489	1.00974	0.99895	0.1636	36.0	0.634	7.19	6.31
608	0.50	1.07364	1.02194	0.99912	0.3062	38.2	0.596	7.65	6.37
629	0.50	1.03912	1.02010	1.00033	0.5097	27.6	0.827	5.51	6.04
606	0.50	1.04022	1.02408	0.99965	0.6022	28.2	0.808	5.64	6.06
611	0.50	1.02717	1.01937	0.99888	0.7243	23.6	0.968	4.71	5.88
613	0.50	1.04355	1.03489	0.99864	0.8072	29.7	0.768	5.94	6.11
703	0.75	1.08599	1.01372	0.99984	0.1611	41.1	0.555	8.22	6.45
620	0.75	1.07465	1.01123	0.99901	0.1616	38.5	0.592	7.70	6.38
618	0.75	1.07104	1.02045	0.99980	0.2899	37.4	0.610	7.47	6.35
615	0.75	1.04439	1.02289	0.99922	0.5240	29.8	0.766	5.95	6.11
619	0.75	1.02831	1.02102	0.99931	0.7486	23.9	0.956	4.77	5.89
628	0.75	1.04727	1.04070	1.00280	0.8523	29.5	0.773	5.90	6.10

**Table 2** Laboratory experimental data for  $\varphi = 0.75$  and  $\Xi = 2.51$ .

Expt.	$\rho_c$ (g/cm <sup>3</sup> )	$\rho_1$ (g/cm <sup>3</sup> )	$\rho_2$ (g/cm <sup>3</sup> )	$S$	$\sqrt{g'h_0}$ (cm/s)	$\frac{\tau_0}{\sqrt{g'h_0}}$ (s)	Re ( $\times 10^4$ )	$\frac{r_u}{r_0}$
719	1.06996	1.01024	0.99947	0.1528	26.3	0.867	2.63	4.75
712	1.06103	1.02017	1.00228	0.3045	24.0	0.951	2.40	4.68
711	1.03998	1.02118	1.00165	0.5095	19.4	1.18	1.94	4.52
716	1.02765	1.01987	1.00129	0.7049	16.1	1.42	1.61	4.38
720	1.04480	1.03803	1.00269	0.8392	20.3	1.12	2.03	4.55

**Table 3** Laboratory experimental data for  $\varphi = 0.5$  and  $\Xi = 1.46$ .

Expt.	$\rho_c$ (g/cm <sup>3</sup> )	$\rho_1$ (g/cm <sup>3</sup> )	$\rho_2$ (g/cm <sup>3</sup> )	$S$	$\sqrt{g'h_0}$ (cm/s)	$\frac{\tau_0}{\sqrt{g'h_0}}$ (s)	Re ( $\times 10^4$ )	$\frac{\tau_c}{\tau_0}$
813	1.07276	1.01006	0.99852	0.1554	33.1	0.690	4.96	5.65
808	1.06599	1.02004	0.99863	0.3178	31.5	0.724	4.72	5.61
803	1.04269	1.02023	0.99873	0.4891	25.4	0.896	3.82	5.41
809	1.02787	1.01929	0.99766	0.7160	21.1	1.08	3.16	5.25
814	1.04531	1.04005	0.99884	0.8868	26.2	0.872	3.92	5.44

**Table 4** Laboratory experimental data for  $\Xi = 1$  and  $S = 0$ .

Expt.	$\rho_c$ (g/cm <sup>3</sup> )	$\rho_2$ (g/cm <sup>3</sup> )	$\sqrt{g'h_0}$ (cm/s)	$\frac{r_0}{\sqrt{g'h_0}}$ (s)	Re ( $\times 10^4$ )	$\frac{r_v}{r_0}$
706a	1.02003	0.99838	20.6	1.11	4.12	5.75
706b	1.01998	0.99868	20.5	1.12	4.09	5.74
706c	1.01930	0.99867	20.1	1.13	4.02	5.73
706d	1.05838	0.99862	34.3	0.666	6.85	6.26
709	1.05655	0.99845	33.8	0.675	6.75	6.24

5. R. Goldman, M. Ungarish, and I. Yavneh. Gravity currents with double stratification: A numerical and analytical investigation. *Environ. Fluid Mech.*, 14:471–499, 2014.
6. J. Y. Holyer and H. E. Huppert. Gravity currents entering a two-layer fluid. *J. Fluid. Mech.*, 100:739–767, 1980.
7. J. W. Rottman and J. E. Simpson. The formation of internal bores in the atmosphere: A laboratory model. *Q. J. R. Meteorol. Soc.*, 115:941–963, 1989.
8. M. R. Flynn, M. Ungarish, and A. W. Tan. Gravity currents in a two-layer stratified ambient: The theory for the steady-state (front condition) and lock-released flows, and experimental confirmations. *Phys. Fluids*, 24:026601, 2012.
9. B. L. White and K. R. Helfrich. A general description of a gravity current front propagating in a two-layer stratified fluid. *J. Fluid Mech.*, 711:545–575, 2012.
10. A. W. Tan, D. S. Nobes, B. A. Fleck, and M. R. Flynn. Gravity currents in two-layer stratified media. *Environ. Fluid Mech.*, 11(2):203–224 (DOI: 10.1007/s10652-010-9174-z), 2011.
11. K. M. Faust and E. J. Plate. Experimental investigation of intrusive gravity currents entering stably stratified fluids. *J. Hydraul. Res.*, 22(5):315–325, 1984.
12. M. Ungarish. Intrusive gravity currents in a stratified ambient – shallow-water theory and numerical results. *J. Fluid Mech.*, 535:287–323, 2005.
13. J. Wu. Mixed region collapse with internal wave generation in a density stratified medium. *J. Fluid Mech.*, 35:531–544, 1969.
14. B. R. Sutherland, P. J. Kyba, and M. R. Flynn. Intrusive gravity currents in two-layer fluids. *J. Fluid Mech.*, 514:327–353, 2004.
15. M. R. Flynn and P. F. Linden. Intrusive gravity currents. *J. Fluid Mech.*, 568:193–202, 2006.
16. J. E. Simpson. *Gravity Currents*. Cambridge University Press, Cambridge, England, 2nd edition, 1997.
17. A. M. Holdsworth, K. J. Barrett, and B. R. Sutherland. Axisymmetric intrusions in two-layer and uniformly stratified environments with and without rotation. *Phys. Fluids*, 24:036603, 2012.
18. M. Ungarish. *An Introduction to Gravity Currents and Intrusions*. CRC Press, Boca Raton, FL, USA, 2009.
19. A. W. Tan. Gravity currents in two-layer stratified media. Master’s thesis, Univ. of Alberta, 2010.
20. T. B. Benjamin. Gravity currents and related phenomena. *J. Fluid Mech.*, 31:209–248, 1968.

- 
21. M. Ungarish. Axisymmetric gravity currents at high Reynolds number - on the quality of shallow-water modeling of experimental observations. *Phys. Fluids*, 19:036602, 2007.
  22. H. E. Huppert and J. E. Simpson. The slumping of gravity currents. *J. Fluid Mech.*, 99:785–799, 1980.
  23. J. M. McMillan and B. R. Sutherland. The lifecycle of axisymmetric internal solitary waves. *Nonlin. Proc. Geophys.*, 17:443–453, 2010.